Chemical Geology xxx (2012) xxx–xxx

Contents lists available at SciVerse ScienceDirect

Chemical Geology

journal homepage: www.elsevier.com/locate/chemgeo

Molecular dynamics simulations of Y in silicate melts and implications for trace element partitioning

Volker Haigis [a,*], Mathieu Salanne [b], Sebastian Simon [a], Max Wilke [a], Sandro Jahn [a]

[a] GFZ German Research Centre for Geosciences, Telegrafenberg, 14473 Potsdam, Germany
[b] UPMC Université Paris 06 and CNRS, UMR 7195, PECSA, 75005 Paris, France

ARTICLE INFO

Article history:
Accepted 22 August 2012
Available online xxxx

Keywords:
Molecular dynamics
Silicate melt
Structure
Trace element partitioning
Thermodynamic integration
EXAFS

ABSTRACT

Element partitioning depends strongly on composition and structure of the involved phases. In this study, we use molecular dynamics simulations to investigate the local environment of Y as an exemplary trace element in four silicate melts with different compositions and thus varying degrees of polymerization. Based on these structural results, we propose a mechanism which explains the observed partitioning trends of Y and other rare-earth elements between crystals and melts or between two melts. With our computational approach, we found a systematic correlation between melt composition and Y coordination as well as Y—O bond lengths, a result which was corroborated by EXAFS spectroscopy on glasses with the same compositions as the simulated melts. Our simulations revealed, moreover, the affinity of Y for network modifiers as second-nearest neighbors (Ca in this study) and the tendency to avoid network formers (Si and Al). This is consistent with the observation that Y (and other rare-earth elements) in general prefer depolymerized to polymerized melts in partitioning experiments (see, e.g., Schmidt et al. (2006)). Furthermore, we used the method of thermodynamic integration to calculate the Gibbs free energy which governs Y partitioning between two exemplary melts. These more quantitative results, too, are in line with the observed partitioning trends.

1. Introduction

In the presence of two or more coexisting phases in thermodynamic equilibrium, a minor or trace element will, in general, not be distributed equally among these phases, but will be incorporated preferentially into some chemical environments at the expense of others. The resulting distribution of an element i between two phases α and β is quantified by the Nernst partition coefficient $D_i^{\alpha/\beta} = c_i^{\alpha}/c_i^{\beta}$, with c_i^{α} denoting the concentration (mass fraction) of element i in phase α. The molar partition coefficient $D_{i*}^{\alpha/\beta} = x_i^{\alpha}/x_i^{\beta}$ is defined in terms of mole fractions x instead of concentrations and can easily be converted to $D_i^{\alpha/\beta}$ (see Beattie et al. (1993), for terminology). The partition coefficient of element i depends, in general, on temperature, pressure, chemical composition and structure of the involved phases. Conversely, if this dependence is known, either from a compilation of experimental data or from a suitable theory, then the distribution of trace elements in, e.g., rock samples can provide information about the petrogenetic history, and hence constitute a valuable tool for petrologists and geochemists (e.g. Shaw (2006)).

Trace element partitioning between coexisting crystal and melt phases can be understood, at least partially, in terms of the local environment of the incorporated cation in the crystal: if the trace element fits available crystal sites well by size and charge, then it is enriched in the crystal, otherwise it partitions into the melt. It has long been known that crystal-melt partition coefficients of a series of isovalent cations, plotted logarithmically as a function of ionic radius, form near-parabolic patterns which peak at an ideal radius (Onuma et al., 1968). These patterns have been described quantitatively by Blundy and Wood (1994) by means of the lattice strain model, based on work by Brice (1975). It translates the strain in the crystal lattice, induced by the mismatch of the incorporated cation, to a free energy penalty for cation incorporation, which in turn governs the partitioning.

The lattice strain model, when suitably parameterized, successfully describes observed crystal-melt partitioning behavior in terms of crystal chemistry alone, without explicitly taking into account melt properties. If the latter are important, their influence on partitioning is hidden in the adjustable model parameters and cannot be predicted nor explained by the original model (although Wood and Blundy (1997) extended the model by taking into account the Mg/(Mg + Fe) ratio in the melt). However, there is broad evidence that melt composition can indeed have a strong effect on trace element partitioning. Prowatke and Klemme (2005), in a series of experiments, measured partition coefficients of several trace elements between titanite ($CaTiSiO_5$) and a range of coexisting silicate melts of different compositions. Although the crystal chemistry was virtually constant in all experiments, partition coefficients varied by two orders of magnitude for several rare-earth elements (REE) and Th. Moreover, the partition coefficients were found to depend

* Corresponding author. Tel.: +49 331 288 28607; fax: +49 331 288 1402.
E-mail address: haigis@gfz-potsdam.de (V. Haigis).

0009-2541/$ – see front matter © 2012 Elsevier B.V. All rights reserved.
http://dx.doi.org/10.1016/j.chemgeo.2012.08.021

systematically on melt polymerization, quantified by the molar ratio of $Al_2O_3/(Na_2O+K_2O+CaO)$. In particular, all the REE probed in the study showed an increasing tendency to partition into the melt the more the melt was depolymerized.

More evidence for the influence of melt composition (and thus melt structure) on element partitioning comes from experiments with immiscible silicate melts (Watson, 1976; Ryerson and Hess, 1978; Schmidt et al., 2006). In the latter study, partition coefficients between coexisting gabbroic (highly depolymerized) and granitic (highly polymerized) melts were determined for a large set of elements. A strong preference of the REE for the depolymerized melt was found, with $D_{REE}^{gabbro/granite} \simeq 10$. According to the authors' interpretation, the abundance of non-bridging oxygen in the depolymerized melt facilitates the formation of the preferred (i.e. energetically favorable) coordination polyhedra of REE and thus favors the observed distribution. In a similar study, Veksler et al. (2006) found the same partitioning trend between immiscible pairs of Fe-rich and Si-rich melt. Mysen (2004) suggested to understand the influence of melt composition on element partitioning in terms of Q^n ($0 \le n \le 4$) species whose abundance and proportions vary with bulk composition, thus offering varying amounts of energetically favorable "sites" for trace element incorporation.

It is the aim of this computational study to elucidate the mechanisms by which melt composition influences the distribution of trace elements between crystal and melt or between two melts. We chose Y as an exemplary REE whose partition behavior was shown to depend strongly on melt properties (Prowatke and Klemme, 2005; Schmidt et al., 2006). From a computational point of view, Y is a more convenient element than the (chemically similar) lanthanides whose strongly correlated *4f* electrons pose notorious problems for theoretical descriptions. Our approach is based on molecular dynamics, a method which provides simultaneous access to the atomic structure and dynamics and to the thermodynamic variables of a system. Taking four different model silicate melts, we first investigated how melt composition influences the local coordination environment of Y ions in the melt. We then translated these structural changes to differences in free energy, which in turn determine the partitioning behavior of Y.

2. Methods

2.1. Interaction potential

We performed molecular dynamics (MD) simulations to investigate structural and thermodynamic properties of silicate melts. Given the considerable system sizes and simulation times required for our study, we did not perform first-principles MD but used a polarizable ionic interaction potential (see Wilson and Madden (1993) for a general discussion) which has been parameterized from first principles (i.e. from fundamental laws of nature, without reference to experimental data), taking density functional theory (DFT, (Hohenberg and Kohn, 1964; Kohn and Sham, 1965)) as a reference. The polarizable ion model is of the form

$$V(\{\mathbf{r}\}) = V^{qq} + V^{rep} + V^{disp} + V^{pol} \tag{1}$$

where $\{\mathbf{r}\}$ represents the set of ionic positions. The first term on the right side describes charge–charge interactions between pairs of ions at $\mathbf{r}_i$ and $\mathbf{r}_j$, with distance $r_{ij}=|\mathbf{r}_i-\mathbf{r}_j|$ and nominal charges q_i and q_j ($q_O=-2$, $q_{Si}=4$, $q_{Ca}=2$, $q_{Al}=q_Y=3$):

$$V^{qq} = \sum_{i<j} \frac{q_i q_j}{r_{ij}} \tag{2}$$

The second term represents the repulsion between two ions due to the overlap of electron densities at short distances:

$$V^{rep} = \sum_{i<j} A_{ij} exp\left(-a_{ij} r_{ij}\right) \tag{3}$$

The A_{ij} and a_{ij} are adjustable model parameters. With the third term, we model dispersion interactions:

$$V^{disp} = -\sum_{i<j} f_6^{ij}\left(r_{ij}\right) \frac{C_6^{ij}}{r_{ij}^6} \tag{4}$$

Here, the C_6^{ij} are calculated from condensed-phase ionic polarizabilities (see below) and the f_6^{ij} represent Tang–Toennies dispersion damping functions which describe deviations from the asymptotic C_6^{ij}/r_{ij}^6 behavior at short distances (Tang and Toennies, 1984) and are defined as

$$f_6^{ij}(r_{ij}) = 1 - exp\left(-b_6^{ij} r_{ij}\right) \sum_{k=0}^{4} \frac{\left(b_6^{ij} r_{ij}\right)^k}{k!} \tag{5}$$

with adjustable parameters b_6^{ij}. The last term in Eq. (1) takes into account the polarizability α of the ions and comprises Coulombic charge–dipole and dipole–dipole interactions as well as a self-energy term which describes the energy cost to polarize an ion:

$$V^{pol} = \sum_{i<j,\alpha} \left[q_i \mu_j^\alpha f_D^{ij}(r_{ij}) - q_j \mu_i^\alpha f_D^{ji}(r_{ji})\right] T_\alpha^{(1)} - \sum_{i<j,\alpha,\beta} \mu_i^\alpha \mu_j^\beta T_{\alpha\beta}^{(2)} + \sum_i \frac{|\mu_i|^2}{2\alpha_i} \tag{6}$$

By μ_i^α, we denote the Cartesian components of ionic dipole moments, and their interaction with ionic charges q_i is damped at short distances by means of Tang–Toennies dipole damping functions $f_D^{ij}(r_{ij})$. These have the same form as in Eq. (5), but now contain the adjustable parameters b_D^{ij} instead of b_6^{ij}. Finally, we write $T_{\alpha\beta\ldots}^{(n)} = \nabla_\alpha \nabla_\beta \cdots 1/r_{ij}$ for the multipole interaction tensors, with the superscript denoting the order of the derivative (Stone, 1996).

We emphasize that the polarization term V^{pol} goes beyond a simple pairwise interaction and introduces real many-body effects. This is because at each MD step, i.e. for given ionic positions $\{\mathbf{r}\}$, all ionic dipole moments are determined self-consistently by minimizing V^{pol} as a function of the dipole moments (Wilson and Madden, 1993), using a conjugate-gradient algorithm. The polarization term turned out to be crucial for a transferable interaction potential for oxides (Rowley et al., 1998). In fact, polarizability mimics a deformable electron density, which is an indispensable ingredient of formally ionic models if they are to describe oxides (or silicates) correctly.

The interaction potential, Eqs. (1) to (6), was parameterized by matching dipoles, forces, and stresses derived from the potential to dipoles, forces, and stresses obtained from DFT, following the procedure presented in Aguado et al. (2003) and Jahn and Madden (2007). As reference configurations, we chose four melt configurations with compositions SiO_2, Al_2O_3, CaO, and Y_2O_3, generated by Born-Oppenheimer MD with at least 80 atoms in the simulation cell. The equilibration runs and the static DFT calculations on the four reference configurations were carried out with the CPMD code (Car and Parrinello, 1985; Marx and Hutter, 2000) within the local density approximation, using Troullier–Martins pseudopotentials (Troullier and Martins, 1991). We found that a plane-wave cutoff of at least 180 Ry (240 Ry for CaO) and a Brillouin zone sampling restricted to Γ produced converged forces, dipoles and stress tensors. The ionic dipoles were calculated from the configuration of maximally localized Wannier functions (Marzari and Vanderbilt, 1997) around ion cores. The model parameters were determined by a least-square fit in a two-step procedure. First, the condensed-phase ionic polarizabilities α_i and all the dipole damping parameters b_D^{ij} were optimized. We treated only O^{2-}, Ca^{2+}, and Y^{3+} as polarizable, and neglected the polarizability of the small cations Si^{4+} and Al^{3+}. Second, keeping these values fixed, the remaining parameters were fitted to DFT forces and stresses. The values of all model parameters are listed in Table 1.

Please cite this article as: Haigis, V., et al., Molecular dynamics simulations of Y in silicate melts and implications for trace element partitioning, Chem. Geol. (2012), http://dx.doi.org/10.1016/j.chemgeo.2012.08.021

To test the accuracy of the new interaction potential, we applied it to $Ca_3(Al,Y)_2(SiO_4)_3$ melt, with one Y atom in the simulation cell, and compared the results to the outcome of a DFT MD run for this system. Since this melt was not among the reference systems used for the fit, we hereby also checked whether the potential is transferable to different chemical compositions. The radial distribution functions for all the cation-oxygen pairs, plotted in Fig. 1, are in excellent agreement with DFT. Melt density constitutes another test of the interaction potential. In an MD simulation at 3000 K and ambient pressure, the density was found to be 2.62 g/cm^3. Unfortunately, no experimental data are available at these conditions, so we resort to the expression given by Lange and Carmichael (1987) for the density of multicomponent silicate melts, which is based on a large experimental data set. At 3000 K, $Ca_3Al_2(SiO_4)_3$ melt is predicted to have a density of 2.45 g/cm^3, 6% lower than our simulation result. This overestimation of density by our interaction potential can be explained by the fact that it has been parameterized with respect to the local density approximation to DFT, which is known to underestimate lattice constants by about 1%–2%, i.e. to overestimate densities by 3%–6%. On the other hand, Lange and Carmichael (1987) caution against using their density formula at temperatures far above 1873 K and indicate that it might underestimate the density of Al-bearing silicate melts at higher temperatures by several percent, so that the difference to our simulated density would be even smaller. In conclusion, the interaction potential has been shown to reproduce DFT-derived melt structures well and to predict melt densities consistent with extrapolations of experimental data.

We close this part of the paper by commenting on the dispersion interaction, the contribution of which to the total potential energy of our model is small, but not negligible. There is no obvious way of obtaining the coefficients C_6^{ij} from DFT calculations, since dispersion is not well described by the available approximate exchange-correlation functionals. However, the coefficients are related to the polarizabilities via the Casimir-Polder integral (Casimir and Polder, 1948) or, in an approximate way, via the Slater-Kirkwood expression (Slater and Kirkwood, 1931)

$$C_6^{ij} = \frac{3}{2}\frac{\alpha_i\alpha_j}{\sqrt{\alpha_i/N_i}+\sqrt{\alpha_j/N_j}} \tag{7}$$

where N_i is a parameter which can be calculated from like-ions interactions and Eq. (7) as

$$N_i = \left[\frac{4}{3}\frac{C_6^{ii}}{\alpha_i^{3/2}}\right]^2 \tag{8}$$

if C_6^{ii} and α_i are known. N_i can then be used in the "combination rule" for unlike ions, Eq. (7). Unfortunately, we don't know the value of $C_6^{O^{2-}-O^{2-}}$ etc. in condensed phases. However, Koutselos and Mason (1986) found empirically that N is nearly constant for ions of an isoelectronic sequence, i.e. $N_{O^{2-}} \simeq N_{Ne}$, etc. Thus we chose the following procedure to determine the coefficients C_6^{ij}: First we calculated N_{Ne}, N_{Ar}, and N_{Kr} from Eq. (8), with gas phase α's and like-ions C_6s obtained from high-level calculations by Chu and Dalgarno (2004). Following Koutselos and Mason (1986), we then assumed $N_{O^{2-}} = N_{Ne}$, $N_{Ca^{2+}} = N_{Ar}$, $N_{Y^{3+}} = N_{Kr}$, and together with the condensed-phase polarizabilities resulting from the dipole-fitting, these yield the required coefficients C_6^{ij}, by Eq. (7). These coefficients, like the dipole parameters, are held constant during the subsequent optimization of the remaining model parameters. Although approximate, the procedure is physically justified and produces reasonable dispersion coefficients.

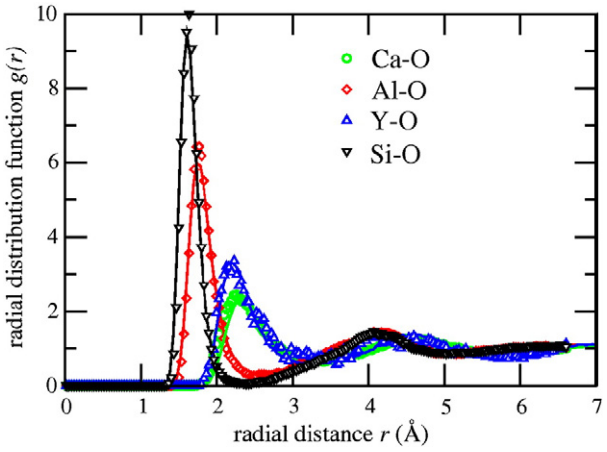

Fig. 1. Radial distribution functions for cation-oxygen pairs in $Ca_3(Al,Y)_2(SiO_4)_3$ melt (grossular composition), at 3000 K and a density of 2.62 g/cm^3. Full lines represent data obtained with the polarizable ion model and symbols are DFT results. The simulation with the polarizable ion model was done with a simulation cell containing one Y atom and 1280 atoms in total. For the DFT-based MD, the simulation cell contained one Y atom and 160 atoms in total, and Born-Oppenheimer MD was performed in the local density approximation, with a plane-wave cut-off of 80 Rydberg.

2.2. Molecular dynamics

Once the interaction potential was parameterized, we performed MD simulations for four silicate melts, of major-element composition Al_2SiO_5, $CaAl_2Si_2O_8$, $Ca_3Al(SiO_4)_3$ and $CaSiO_3$. The cubic simulation cells, repeated periodically in space, contained 1152, 1664, 1280 and 1079 atoms, respectively, with one Al^{3+} replaced by Y^{3+} (three CaO replaced by Y_2O_3 in the case of $CaSiO_3$). The atoms were first placed randomly into the cells, which were then equilibrated for at least 20 ps at 3000 K and ambient pressure. Temperature and pressure were controlled by a Nosé–Hoover thermostat (Nosé, 1984; Hoover, 1985) and a barostat (Martyna et al., 1994), respectively. We then fixed the volume of the simulation cell to the average volume of the last 10 ps and equilibrated the systems during another 10 ps, now at constant volume and temperature $T = 3000$ K (*NVT* ensemble). Data were acquired during subsequent *NVT* simulations of 100 ps duration, using a time step of 1 fs for the integration of the Newtonian equations of motion. The structural results obtained from the MD simulations (coordination numbers, bond lengths) are well-converged with respect to the run duration, since virtually the

Table 1
Interaction parameters, see Eqs. (1) to (6), in atomic units. Interactions not listed or left blank here, e.g., short-range repulsion for Si–Si, are taken to be absent in the model. Since $b_D^{ij} \neq b_D^{ji}$ in general, both parameters are listed.

i–j	O—O	Si—O	Al—O	Ca—O	Y—O	Ca—Ca	Y—Y	Ca—Y
q_i	−2	+4	+3	+2	+3			
A_{ij}	5328.3	44.624	39.404	76.811	95.048			
a_{ij}	3.1526	1.6513	1.6413	1.7038	1.6813			
C_6^{ij}	52.461			16.716	23.763	6.4724	12.504	8.9817
b_6^{ij}	2.7370			1.7543	1.4995	2.8594	0.67066	1.0865
α_i	10.754			2.4116	3.5475			
b_D^{ij}	0.0	1.6489	1.5573	1.4304 (Ca—O)/ 3.4741 (O—Ca)	1.5056 (Y—O)/ 3.3585 (O—Y)			

Please cite this article as: Haigis, V., et al., Molecular dynamics simulations of Y in silicate melts and implications for trace element partitioning, Chem. Geol. (2012), http://dx.doi.org/10.1016/j.chemgeo.2012.08.021

same values result from analysis of the last 50 ps only of each simulation. For the first three compositions, since there was only one Y atom per cell, the interaction with other Y atoms (periodic images in other cells) was very weak, given a minimum distance of 23.5 Å. For $CaSiO_3$, we checked that the two Y atoms in the simulation cell did not form a complex during the simulation. Hence, we expect Y to behave as a trace element in all simulations.

2.3. Thermodynamic integration

Trace element partitioning is ultimately driven by the tendency of any thermodynamic system to minimize its free energy. Whereas the internal energy U of a system is readily obtained from MD simulations, free energies cannot be extracted directly from a single simulation (note that also in experiments, free energies cannot be determined from a single measurement, in contrast to quantities like temperature or pressure). However, the method of thermodynamic integration can be used to derive free energy differences from MD (Frenkel and Smit, 2002). We applied this method to calculate the change in Gibbs free energy associated with an exchange reaction of Y and Al between two silicate melts:

$$\begin{aligned} &Y^{3+} \text{ in melt } 1 + Al^{3+} \text{ in melt } 2 \\ &\rightleftharpoons Al^{3+} \text{ in melt } 1 + Y^{3+} \text{ in melt } 2 \end{aligned} \tag{9}$$

The equilibrium constant K of this reaction is related to the molar exchange coefficient $K_{D,Y/Al}^{m2/m1}$ (see Beattie et al. (1993) for terminology):

$$K = \frac{a_{Al}^{m1} a_{Y}^{m2}}{a_{Y}^{m1} a_{Al}^{m2}} \simeq \frac{x_{Al}^{m1} x_{Y}^{m2}}{x_{Y}^{m1} x_{Al}^{m2}} = \frac{D_{Y*}^{m2/m1}}{D_{Al*}^{m2/m1}} = K_{D,Y/Al}^{m2/m1} \tag{10}$$

Here, m1 and m2 stand for the two melts, of different composition. The exchange coefficient is just the partition coefficient of Y, normalized by the one of Al, and thus quantifies the fractionation of Y and Al between the melts. We assumed that activities a can be replaced by mole fractions x in Eq. (10).

For computational purposes, we split the exchange reaction (9) into two partial reactions, or "transmutations",

$$\begin{aligned} &Y^{3+} \text{ in melt } 1 \rightleftharpoons Al^{3+} \text{ in melt } 1 \\ &Al^{3+} \text{ in melt } 2 \rightleftharpoons Y^{3+} \text{ in melt } 2 \end{aligned} \tag{11}$$

The reason for this splitting is that we can compute the change in Gibbs free energy for each of the two partial reactions by means of thermodynamic integration, following the procedure described by Salanne et al. (2008) and outlined in the next paragraph. With this method, the interaction parameters of Y are gradually transformed into those of Al (or vice versa). Although the two reactions in Eq. (11) do not correspond to real physical processes, the associated free energy differences are well defined, and taken together, they give the complete (physical) exchange reaction (9). The total change in Gibbs free energy, ΔG, for the reaction (9) determines the equilibrium constant $K = exp(-\Delta G/(RT))$ and thus the exchange coefficient through Eq. (10).

In more technical terms, in order to describe the transmutations, we introduce a hybrid potential energy function, characterizing a system in which one Y atom is partially transmuted into Al. It is defined as a linear mixture of two potential energy functions of the same form as in Eq. (1):

$$V_\lambda(\{\mathbf{r}\}) = (1-\lambda)V_Y(\{\mathbf{r}\}) + \lambda V_{Al}(\{\mathbf{r}\}) \tag{12}$$

Here, V_Y is the potential energy of the system (melt) containing one Y^{3+}, and V_{Al} is the potential energy of a system where Y^{3+} is replaced by Al^{3+}. The parameter λ takes values between 0 (the atom in question is pure Y) and 1 (the atom is fully transmuted into Al). Now, following an idea of Kirkwood (1935), we express the free energy change for the "reaction" $Y^{3+} \rightarrow Al^{3+}$ in a given melt (one of the transmutations in Eq. (11)) as

$$\Delta G = \int_0^1 \left\langle \frac{\partial V_\lambda}{\partial \lambda} \right\rangle_\lambda d\lambda = \int_0^1 \langle V_{Al} - V_Y \rangle_\lambda d\lambda \tag{13}$$

where $\langle \ldots \rangle_\lambda$ denotes the average in a system governed by the hybrid potential energy function V_λ. The crucial point of the method is that the difference $V_{Al}(\{\mathbf{r}\}) - V_Y(\{\mathbf{r}\})$ is a known function of the atomic coordinates, and hence its average can be computed directly from an MD trajectory, unlike ΔG itself. If $\langle V_{Al} - V_Y \rangle_\lambda$ is evaluated by means of several MD simulations for a set of λ values, the free energy of reaction (transmutation) can be obtained by numerical integration according to Eq. (13).

The simulations were carried out by means of the CP2K code (http://cp2k.berlios.de/). As melt compositions m1 and m2, we chose Al_2SiO_5 and $CaAl_2Si_2O_8$, with supercells containing 22 formula units in the case of Al_2SiO_5 and 16 formula units in the case of $CaAl_2Si_2O_8$. Both systems were equilibrated at 2500 K and ambient pressure, and data were acquired at constant volume (corresponding to ambient pressure) and with a Nosé–Hoover thermostat maintaining the temperature at 2500 K. In each system, Al was gradually transformed into Y in five steps, and at each intermediate step, we performed a full MD of 12 ps duration, starting from the final configuration of the previous run. Of these 12 ps, the first 2 ps served for equilibration after slightly changing the interaction potential V_λ, and the remaining 10 ps were used for analysis. After a full transmutation from Al to Y, we also simulated the reverse transmutation from Y to Al. The sum of free energy changes, $\Delta G_{forward} + \Delta G_{backward}$, of the forward and the backward transmutation (which should ideally be zero since it represents a null reaction) was used to estimate the error due to incomplete sampling of the phase space.

Since periodic boundary conditions were applied, the question arises how the finite size of the simulation cell influences the calculated free energy differences. We expect that the respective error is below 5%, for the following reason: Ayala and Sprik (2008) carefully studied the finite-size effect on the free energy change associated with a redox reaction of a single metal cation in water, using thermodynamic integration as well. They found that free energies were converged to <5% with respect to the limit of very large cells, for cell sizes comparable to ours. Now, in their study, the transmutation involves a change of the cationic charge ($M^{2+} \rightleftharpoons M^{3+}$), whereas in our case, only the short-range interaction and the less significant polarizability and van der Waals parameters are changed ($Y^{3+} \rightleftharpoons Al^{3+}$). Therefore, the effect of limited cell sizes should be even less important here than in the redox case, where changes in strong, long-range Coulomb interactions occur.

3. Results and discussion

3.1. Atomic environment of Y in silicate melts from MD simulations

The four melt compositions, Al_2SiO_5, $CaAl_2Si_2O_8$, $Ca_3Al_2(SiO_4)_3$ and $CaSiO_3$, were selected in such a way as to span a wide range of melt polymerization. As a simple compositional variable, we chose the ratio of non-bridging oxygens to the total amount of Si and Al, NBO/(Si + Al), which was obtained from the simulations. For the present study, we prefer this terminology to the more standard NBO/T (T = tetrahedrally coordinated network former) because the average coordination of Al was found to be larger than 4, even in nominally fully polymerized melts, and thus Al cannot always be classified as T. We still suggest to view NBO/(Si + Al) as a measure of melt depolymerization, with Ca acting as a network modifier. Non-bridging oxygen is defined here as oxygen which is not exclusively bonded to Si or Al, according to the bonding criterion presented in the following paragraph.

Please cite this article as: Haigis, V., et al., Molecular dynamics simulations of Y in silicate melts and implications for trace element partitioning, Chem. Geol. (2012), http://dx.doi.org/10.1016/j.chemgeo.2012.08.021

Coordination numbers and average bond lengths were obtained from the simulations in the following way: for a given pair of elements *i*– *j*, we calculated the radial pair distribution function $g(r_{ij})$ by organizing the various *i*–*j* distances occurring during the simulation into bins and suitably normalizing the resulting distribution (see, e.g., Fig. 1). We then fixed the cut-off radius r_{cut} for this element pair at the distance where $g(r_{ij})$ adopts its first minimum, i.e. r_{cut} represents the radial extent of the first coordination shell. The coordination of element *i* by element *j* is determined by averaging, over all *i*-atoms and over the duration of the simulation, the number of *j*-atoms closer to a given *i*-atom than r_{cut}. Similarly, the average *i*-*j* bond length is obtained as the average distance r_{ij} of atom pairs with a distance less than r_{cut}. Note that in general, r_{cut} for a given element pair varies with melt composition, which reflects changes in the shape of the first coordination shell.

As a first step towards understanding the atomistic mechanisms leading to trace element partitioning between melts, we investigated how the local environment of Y changes as a function of melt composition. Fig. 2 shows that the coordination of Y by O drops from 7.7 in Al_2SiO_5 (which has NBO/(Si + Al) = 0.0) to 6.2 in $CaSiO_3$ (NBO/(Si + Al) = 1.9). Concurrently, the average distance between Y and its nearest-neighbor oxygen decreases from 2.56 Å to 2.46 Å, as can be seen from Fig. 3. Coordination numbers and average Y—O distances are also listed in Table 2. In Fig. 4, the radial distribution of oxygen atoms around Y is plotted for the four different melt compositions. We observe that with increasing NBO/(Si + Al), the distribution becomes narrower, or in other words, oxygen disorder around Y decreases. The peak position does not exhibit systematic changes, except for the case of Al_2SiO_5, where it is shifted to larger Y—O distances. For the other three compositions, the height of the peak increases with increasing NBO/(Si + Al). These data imply that the observed decrease of coordination number and Y—O bond length with decreasing polymerization is largely due to the reduction of the tail of the distribution at large Y—O distances.

In order to gain further insight into structural differences resulting from changes in composition, we also investigated the chemical composition of the second coordination shell around Y. In Fig. 5, we plot the average number of cations bonded to one oxygen atom if the latter is itself bonded to Y. Oxygen-cation bonding statistics were again based on cut-off radii obtained from the simulations. As expected from the bulk melt composition, the amount of Ca in the second shell increases at the expense of Si and Al, when going to the more depolymerized, i.e. more Ca-rich compositions. The essential result, however, is that for all Ca-bearing melts, the ratio Ca/(Si + Al) in the second coordination shell is *larger* than the bulk ratio, i.e. Y tends to be associated with the network modifier Ca rather than with Si or Al.

In the light of these structural findings, we put forward a qualitative explanation of the observed partitioning of Y in terms of its bonding requirement. Whereas Si and Al form very strong bonds with oxygen, the Ca—O bonds have a looser character, since Ca is less charged and has a greater ionic radius than Si and Al. When trying to satisfy its bonding requirements, Y competes for oxygen bonds with other cations. In a polymerized melt, many strong competitors (Si and Al) are present, and Y has to take what is left, forming many weak (elongated) bonds. On the other hand, in the presence of weak competitors like Ca, Y can shape its bonding environment according to its needs and forms less, but stronger (shorter) bonds. The enhanced ability of Y to shape its environment is reflected by the reduced oxygen disorder around Y, which is indicated by the narrower Y—O distribution shown in Fig. 4, as discussed above. This picture explains the trends in coordination number and average Y—O distance seen in the simulations. The fact that Y prefers to be associated with Ca instead of Si and Al in the second coordination shell indicates that it is energetically more favorable for Y to be surrounded by weak competitors. This should lead to the observed partitioning into the more depolymerized melts. In Section 3.3, we will take a more quantitative approach to the energetics of trace element partitioning.

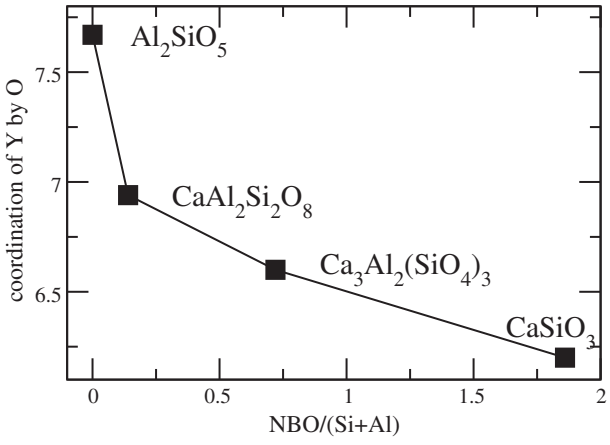

Fig. 2. Coordination number of Y by O as a function of melt composition, NBO/(Si + Al) from simulation. Lines are a guide to the eye.

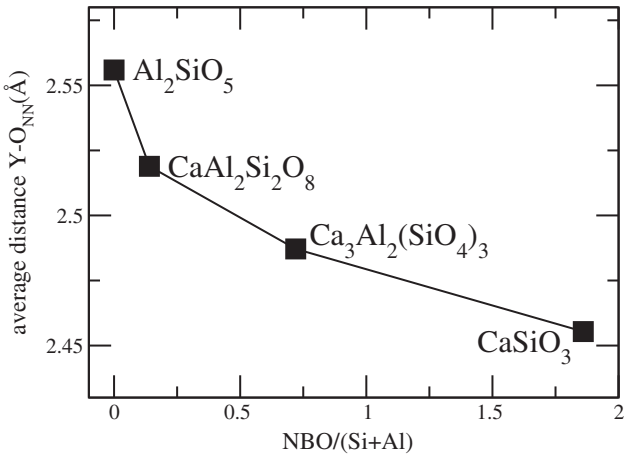

Fig. 3. Average nearest-neighbor (NN) Y—O bond length as a function of melt composition, NBO/(Si + Al) from simulation. Lines are a guide to the eye.

3.2. Comparison to EXAFS experiments

To corroborate our structural findings obtained from MD simulations, we compared them to results from extended x-ray absorption fine structure (EXAFS) spectroscopy at the Y K-edge on four glasses

Table 2
Structural parameters for Y in silicate melts (glasses): coordination number CN, cut-off radius r_{cut} for CN in Å and average Y—O distance $\overline{d}$ in Å, with standard deviations in parentheses. Simulations performed at 3000 K, EXAFS spectra taken on glasses at 300 K. *CN fixed at simulation values, see text for explanation.

	Simulation	Experiment
Al_2SiO_5		
CN	7.7	–
r_{cut}	3.24	
$\overline{d}$	2.56	–
$CaAl_2Si_2O_8$		
CN	6.9	6.9*
r_{cut}	3.24	
$\overline{d}$	2.52	2.34 (0.01)
$Ca_3Al_2(SiO_4)_3$		
CN	6.6	6.6*
r_{cut}	3.25	
$\overline{d}$	2.49	2.31 (0.01)
$CaSiO_3$		
CN	6.2	6.2*
r_{cut}	3.22	
$\overline{d}$	2.46	2.28 (0.01)

Please cite this article as: Haigis, V., et al., Molecular dynamics simulations of Y in silicate melts and implications for trace element partitioning, Chem. Geol. (2012), http://dx.doi.org/10.1016/j.chemgeo.2012.08.021

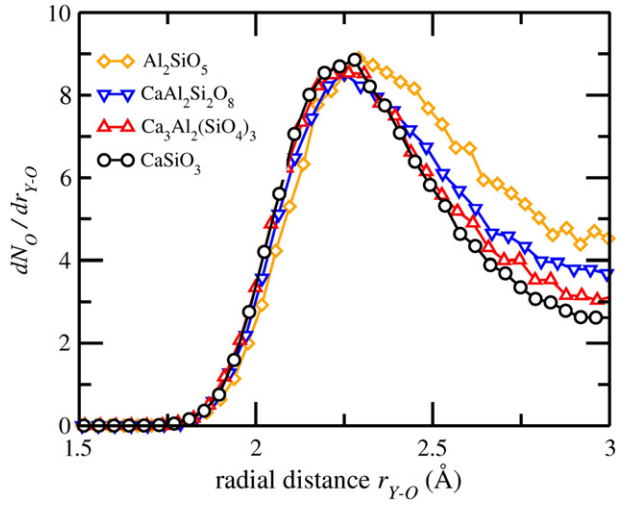

Fig. 4. Distribution of O around Y in four silicate melts as obtained from MD simulation. The area under a curve up to a certain distance r_{Y-O} gives the number N_O of oxygen atoms within a sphere of radius r_{Y-O} around Y. Lines are a guide to the eye.

of the same major-element composition as the four simulated silicate melts, doped with 5000 ppm of Y. EXAFS probes the local environment around a selected element and hence provides information about the first coordination shell of O around Y, in particular about the average Y—O distance. Since the spectra taken on Al_2SiO_5 glass could not be interpreted satisfactorily, this composition was excluded from further analysis. The details of synthesis, sample preparation, data acquisition and analysis are described by Simon et al.

A difficulty arises from the fact that the experiments were performed on glasses at room temperature whereas the simulations describe melts at 3000 K. Apart from one case (see below), we did not perform extensive simulations of glasses at room temperature (which could be compared directly to the EXAFS data) because MD averages are physically meaningful only to the extent that the simulated system samples all of the energetically relevant phase space. For a single Y atom in glassy silicates, this criterion is not fulfilled at low temperatures and with tractable simulation box sizes and simulation lengths. On the other hand, *in situ* EXAFS measurements on melts are experimentally very challenging (Pauvert et al., 2010). We anticipate that absolute interatomic distances will be larger in the high-temperature melt than in the glass, due to thermal expansion, but expect *changes* between different compositions to be similar for melts and glasses.

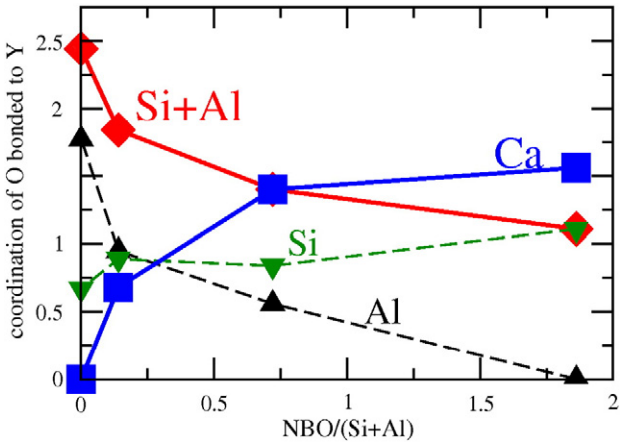

Fig. 5. Chemical composition of the second (cationic) coordination shell around Y as a function of melt composition: number of cations per first-shell O. Lines are a guide to the eye.

The Y—O distance resulting from the analysis of the EXAFS data are compared to the results from the simulations in Table 2. For the analysis of the EXAFS data, the coordination of Y was taken to be the one found in the MD simulations (see Simon et al. in this issue for a discussion). As expected, we find Y—O bonds systematically elongated by about 8% in the high-temperature simulation with respect to the data extracted from EXAFS. But remarkably, the Y—O bond length decreases consistently by 0.06 Å in both simulation and experiment, when going from the more polymerized $CaAl_2Si_2O_8$ to the more depolymerized $CaSiO_3$. For the distribution of O around Y, the experimental data reveal the same trend as the MD simulations: with increasing NBO/(Si + Al), the peak becomes narrower and higher, reflecting increasing oxygen order around Y (Fig. 6). As expected, these distributions, measured on glasses, are significantly narrower and more pronounced than the ones obtained from the simulation of high-temperature melts (Fig. 4). Note, however, that they sum up to the same coordination numbers. The agreement in change of Y—O bond length between simulation and experiment as well as the congruent changes in the shape of the distribution suggest that our interaction model for MD correctly captures the link between melt composition and local environment around Y.

In order to confirm that the observed differences between simulation and experiment are largely due to differences between melts and glasses, and not to deficiencies of our interaction potential, we also simulated $Ca_3Al_2(SiO_4)_3$ glass, containing a single Y atom, at 300 K. We circumvented the problem of insufficient sampling of the phase space by running a simulation at 3000 K, picking 100 configurations from this simulation and quenching them separately to 300 K. With this procedure, different Y environments (sampled in the high-temperature run) are "frozen" into the glass structures, and the average over the 100 resulting glass structures should yield a representative description of Y in $Ca_3Al_2(SiO_4)_3$ glass. Note however, that due to the limited simulation time, the quench rate in the simulation was -2.5×10^{11} K/s, much larger than in the experiments. This means that the simulated glass formed at a higher fictive temperature and therefore probably still has a slightly different structure than the glass analyzed by EXAFS spectroscopy. We found an average Y—O distance of 2.38 Å in the simulated glass, to be compared with 2.31 Å obtained from experiment (and 2.49 Å in the simulated melt at 3000 K). The coordination number of Y was found to be 6.1 (compared to 6.6 in the melt). The satisfying agreement with experiment further

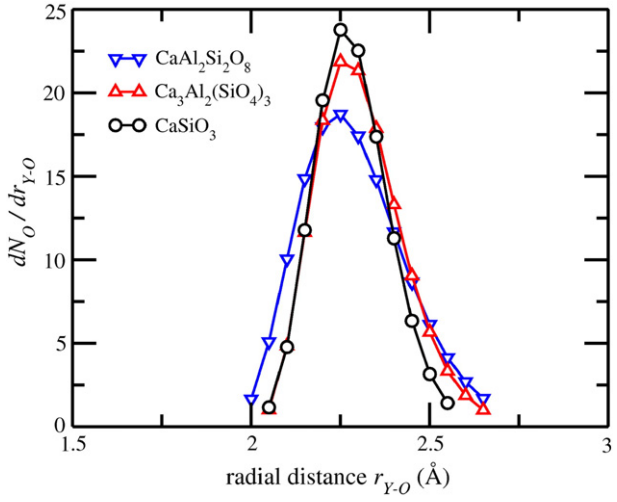

Fig. 6. Distribution of O around Y in three silicate melts as obtained from EXAFS spectroscopy (for details see Simon et al. in this issue). The area under a curve up to a certain distance r_{Y-O} gives the number N_O of oxygen atoms within a sphere of radius r_{Y-O} around Y. Note the change of scale of the ordinate axis with respect to Fig. 4. Lines are a guide to the eye.

Please cite this article as: Haigis, V., et al., Molecular dynamics simulations of Y in silicate melts and implications for trace element partitioning, Chem. Geol. (2012), http://dx.doi.org/10.1016/j.chemgeo.2012.08.021

corroborates the adequacy of our interaction potential in predicting glass and melt structures.

3.3. Y partitioning between silicate melts

In Section 3.1, we suggested a qualitative explanation for the preference of Y for less polymerized melts in terms of competition for bonding. Now we turn to a more quantitative description of element partitioning and consider the free energy balance which accompanies the process. For trace element incorporation in crystals, the lattice strain model (Blundy and Wood, 1994) provides a link between the structural changes induced by the incorporation (strain) and the associated energy costs, and these determine the influence of the crystal on partitioning. However, in melts, there is no such obvious link, due to the lack of well-defined lattice sites. We therefore chose a more general approach and applied the method of thermodynamic integration, by which we calculated the change in Gibbs free energy upon replacing a major element cation in the melt (Al) by a trace element (Y), and like in crystals, this change in Gibbs free energy governs partitioning. More precisely, we modeled the exchange reaction of Y^{3+} and Al^{3+} between Al_2SiO_5 melt and $CaAl_2Si_2O_8$ melt, as described in Section 2.3:

$$Y^{3+} \text{ in } Al_2SiO_5 + Al^{3+} \text{ in } CaAl_2Si_2O_8 \rightleftharpoons Al^{3+} \text{ in } Al_2SiO_5 + Y^{3+} \text{ in } CaAl_2Si_2O_8 \quad (14)$$

By choosing this melt pair, we by no means want to suggest that these melts coexist as immiscible phases in nature or experiment. Rather they serve as a simplified model system on which the mechanism and the energetics of trace element distribution can be studied. Moreover, even hypothetical partitioning between two melts provides information about partitioning between mineral and melt: if one is interested in the *relative change* of trace element distribution between a mineral (with constant chemistry) and melts of varying compositions (see, e.g., Prowatke and Klemme (2005)), the problem can be reduced to partitioning between the different melts, because the contribution of the mineral cancels out. The equilibrium constant of reaction (14) is well-defined thermodynamically and reflects the fractionation tendency of Y and Al between the two melts. We suggest to view Al_2SiO_5 as highly polymerized in the sense that the ratio NBO/(Si + Al) is 0, whereas for $CaAl_2Si_2O_8$, we found NBO/(Si + Al) = 0.14 in the simulation and thus consider it less polymerized (although nominally fully polymerized). The presence of a significant amount of NBO in glasses of this composition has also been comfirmed by NMR experiments (Stebbins and Xu, 1997).

The thermodynamic integration was carried out numerically, interpolating the five data points, corresponding to five values of λ, for each system with a 4th order polynomial (Fig. 7). The change in free energy for the transmutation $Y^{3+} \rightarrow Al^{3+}$ is given by the integral in Eq. (13), i.e. the area between a curve and the *x* axis, and is found to be negative in both Al_2SiO_5 and $CaAl_2Si_2O_8$ (areas below the *x* axis are counted as negative). This indicates that incorporation of Y is energetically less favorable in both cases than incorporation of Al. However, in Al_2SiO_5, it is unfavorable to a higher degree, and thus the overall minimization of the Gibbs free energy dictates partitioning of Y into $CaAl_2Si_2O_8$.

Quantitatively, we obtained a total $\Delta G = (-66 \pm 2)$ kJ/mol for the reaction (14). The negative sign indicates that the equilibrium is shifted to the right side, with Al enriched in the highly polymerized Al_2SiO_5 melt and Y incorporated preferentially into the less polymerized, Ca-bearing $CaAl_2Si_2O_8$. For $T = 2500$ K, the resulting equilibrium constant is $K = 24 \pm 2$. According to Eq. (10), it approximates the ratio of molar partition coefficients $D_{Y*}^{m2/m1}/D_{Al*}^{m2/m1}$ with m1 and m2 representing Al_2SiO_5 and $CaAl_2Si_2O_8$, respectively. If one assumes that ΔG does not vary a lot with temperature, the equilibrium constant will be $K = (200 \pm 30)$ at 1500 K, a temperature in the range usually covered in experiments.

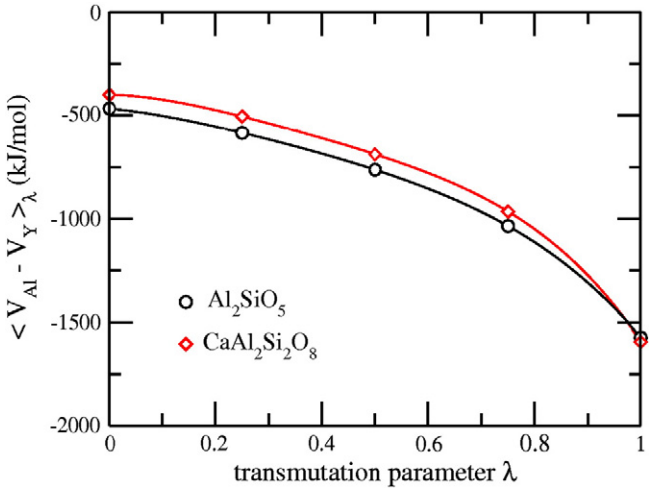

Fig. 7. Thermodynamic integration for the exchange reaction of Y and Al between Al_2SiO_5 and $CaAl_2Si_2O_8$ melt (Eq. (13)). The data points represent the average potential energy difference $\langle V_{Al} - V_Y \rangle_\lambda$ for the two compositions as a function of the transmutation parameter λ. The curves are 4th order polynomial interpolations to the data. Either of the curves represents one of the transmutations or partial reactions in Eq. (11). The area between the two curves corresponds to the total change in Gibbs free energy, ΔG, for the complete exchange reaction.

Since the equilibrium constant of the exchange reaction (14) is related to a *ratio* of partition coefficients, we are cautious with making statements about $D_{Y*}^{m2/m1}$ itself. However, Veksler et al. (2006) found that the partition coefficients of Al between two immiscible silicate melts are not too far from 1 (and much closer to unity than the partition coefficients of REE). If we assume that this also holds for our system, then our result indicates $D_{Y*}^{m2/m1} > 1$. This finding is in agreement with the observed preference of Y (and other REE) for more depolymerized melts. It is also in line with our interpretation of the structural data in Section 3.1, where we argued that the presence of Ca (a "weak competitor") facilitates the incorporation of Y into the melt.

4. Conclusions

We combined MD simulations and EXAFS spectroscopy to investigate the structural environment of Y as a trace element in silicate melts of varying composition. For the MD, a new interaction potential including polarization was constructed for the system Y—Ca—Al—Si—O, which proved to be accurate, transferable and computationally efficient. The simulations revealed two structural trends: First, the average coordination number of Y decreases when the melt polymerization decreases (i.e. when the Ca content increases). This change is accompanied by a decrease of the average Y—O distance by about 4%, and at the same time, oxygen disorder around Y is reduced. A very similar variation is also seen in EXAFS experiments on glasses, which corroborates the reliability of the simulation results.

Second, the MD simulations for the three Ca-bearing melts indicate that the second (cationic) coordination shell around Y exhibits a larger Ca/(Si + Al) ratio than the bulk composition. In other words, Y tends to form clusters with the network modifier Ca, which implies that for a given melt, it is energetically more favorable for Y to share oxygen with Ca than with the network formers Si and Al. This, in turn, suggests that, given *two* melts of different composition, Y should partition preferentially into the one with larger Ca/(Si + Al) ratio, i.e. into the less polymerized melt. Indeed, modeling the exchange reaction of Y and Al between a Ca-free and a Ca-bearing melt by means of thermodynamic integration, we confirmed that minimization of Gibbs free energy drives Y into the Ca-bearing melt.

Please cite this article as: Haigis, V., et al., Molecular dynamics simulations of Y in silicate melts and implications for trace element partitioning, Chem. Geol. (2012), http://dx.doi.org/10.1016/j.chemgeo.2012.08.021

In summary, using simple systems, we presented computational and experimental evidence on how the influence of melt composition on trace element partitioning can be rationalized in terms of atomic-scale processes. We found a systematic influence of melt composition on the microscopic melt structure around Y and investigated the energetic implications of structural changes. The exemplary result that Y incorporation into melts is facilitated by the presence of network modifiers is consistent with the general observation that REE prefer depolymerized melts to polymerized ones. Although most systems which are studied experimentally, and Nature itself, are more complex than the melts investigated in this study, we still hold that the underlying mechanisms are the same in both cases.

Acknowledgments

This work was funded by the German Research Foundation DFG (grants JA1469/4-1 and WI2000/6-1). The calculations were in part performed on JUROPA and JUGENE at the Jülich Supercomputing Centre under the NIC project grant HPO15. Part of the work was carried out under the HPC-EUROPA2 project (project number: 228398) with the support of the European Commission Capacities Area — Research Infrastructures Initiative. We also acknowledge support from DAAD-PROCOPE under grant no. D/9811428.

References

Aguado, A., Bernasconi, L., Jahn, S., Madden, P.A., 2003. Multipoles and interaction potentials in ionic materials from planewave-DFT calculations. Faraday Discussions 124, 171–184.

Ayala, R., Sprik, M., 2008. A classical point charge model study of system size dependence of oxidation and reorganization free energies in aqueous solutions. The Journal of Physical Chemistry 112, 257–269.

Beattie, P., Drake, M., Jones, J., Leeman, W., Longhi, J., McKay, G., Nielsen, R., Palme, H., Shaw, D., Takahashi, E., Watson, B., 1993. Terminology for trace-element partitioning. Geochimica et Cosmochimica Acta 57, 1605–1606.

Blundy, J., Wood, B., 1994. Prediction of crystal-melt partition coefficients from elastic moduli. Nature 372, 452–454.

Brice, J.C., 1975. Some thermodynamic aspects of the growth of strained crystals. Journal of Crystal Growth 28, 249–253.

Car, R., Parrinello, M., 1985. Unified approach for molecular dynamics and density-functional theory. Physical Review Letters 55, 2471–2474.

Casimir, H.B.G., Polder, D., 1948. The influence of retardation on the London-van der Waals forces. Physical Review 73, 360–372.

Chu, X., Dalgarno, A., 2004. Linear response time-dependent density functional theory for van der Waals forces. The Journal of Chemical Physics 121, 4083–4088.

Frenkel, D., Smit, B., 2002. Understanding Molecular Simulation: From Algorithms to Applications. Academic Press, San Diego.

Hohenberg, P., Kohn, W., 1964. Inhomogeneous electron gas. Physical Review 136, B864–B871.

Hoover, W.G., 1985. Canonical dynamics: equilibrium phase-space distributions. Physical Review A 31, 1695–1697.

Jahn, S., Madden, P.A., 2007. Modeling Earth materials from crustal to lower mantle conditions: a transferable set of interaction potentials for the CMAS system. Physics of the Earth and Planetary Interiors 162, 129–139.

Kirkwood, J.G., 1935. Statistical mechanics of fluid mixtures. The Journal of Chemical Physics 3, 300–313.

Kohn, W., Sham, L.J., 1965. Self-consistent equations including exchange and correlation effects. Physical Review 140, A1133–A1138.

Koutselos, A.D., Mason, E.A., 1986. Correlation and prediction of dispersion coefficients for isoelectronic systems. The Journal of Chemical Physics 85, 2154–2160.

Lange, R.A., Carmichael, I.S.E., 1987. Densities of $Na_2O-K_2O-CaO-MgO-FeO-Fe_2O_3-Al_2O_3-TiO_2-SiO_2$ liquids: new measurements and derived partial molar properties. Geochimica et Cosmochimica Acta 51, 2931–2946.

Martyna, G.J., Tobias, D.J., Klein, M.L., 1994. Constant pressure molecular dynamics algorithms. The Journal of Chemical Physics 101, 4177–4189.

Marx, D., Hutter, J., 2000. Ab Initio Molecular Dynamics: Theory and Implementation. In: Grotendorst, J. (Ed.), Modern Methods and Algorithms of Quantum Chemistry. NIC Series, vol. 1. Forschungszentrum Jülich, pp. 301–449.

Marzari, N., Vanderbilt, D., 1997. Maximally localized generalized Wannier functions for composite energy bands. Physical Review B 56, 12847–12865.

Mysen, B.O., 2004. Element partitioning between minerals and melts, melt composition, and melt structure. Chemical Geology 213, 1–16.

Nosé, S., 1984. A molecular dynamics method for simulations in the canonical ensemble. Molecular Physics 52, 255–268.

Onuma, N., Higuchi, H., Wakita, H., Nagasawa, H., 1968. Trace element partition between two pyroxenes and the host lava. Earth and Planetary Science Letters 5, 47–51.

Pauvert, O., Zanghi, D., Salanne, M., Simon, C., Rakhmatullin, A., Matsuura, H., Okamoto, Y., Vivet, F., Bessada, C., 2010. In situ experimental evidence for a nonmonotonous structural evolution with composition in the molten LiF-ZrF_4 System. The Journal of Physical Chemistry. B 114, 6472–6479.

Prowatke, S., Klemme, S., 2005. Effect of melt composition on the partitioning of trace elements between titanite and silicate melt. Geochimica et Cosmochimica Acta 69, 695–709.

Rowley, A.J., Jemmer, P., Wilson, M., Madden, P.A., 1998. Evaluation of the many-body contributions to the interionic interactions in MgO. The Journal of Chemical Physics 108, 10209–10219.

Ryerson, F.J., Hess, P.C., 1978. Implications of liquid-liquid distribution coefficients to mineral-melt partitioning. Geochimica et Cosmochimica Acta 42, 921–932.

Salanne, M., Simon, C., Turq, P., 2008. Calculation of activities of ions in molten salts with potential application to the pyroprocessing of nuclear waste. The Journal of Physical Chemistry 112, 1177–1183.

Schmidt, M.W., Connolly, J.A.D., Günther, D., Bogaerts, M., 2006. Element partitioning: the role of melt structure and composition. Science 312, 1646–1650.

Shaw, D.M., 2006. Trace Elements in Magmas. A Theoretical Treatment. Cambridge University Press, Cambridge.

Simon, S., Wilke, M., Chernikov, R., Klemme, S., Hennet, L., this issue. The influence of composition on the local structure around yttrium in quenched silicate melts - insights from EXAFS. Chemical Geology xxx, xxx–xxx.

Slater, J.C., Kirkwood, J.G., 1931. The van der Waals forces in gases. Physical Review 37, 682–697.

Stebbins, J.F., Xu, Z., 1997. NMR evidence for excess non-bridging oxygen in an aluminosilicate glass. Nature 390, 60–62.

Stone, A.J., 1996. The Theory of Intermolecular Forces. Oxford University Press Inc., New York.

Tang, K.T., Toennies, J.P., 1984. An improved simple model for the van der Waals potential based on universal damping functions for the dispersion coefficients. The Journal of Chemical Physics 80, 3726–3741.

Troullier, N., Martins, J.L., 1991. Efficient pseudopotentials for plane-wave calculations. Physical Review B 43, 1993–2005.

Veksler, I.V., Dorfmann, A.M., Danyushevsky, L.V., Jakobsen, J.K., Dingwell, D.B., 2006. Immiscible silicate liquid partition coefficients: implications for crystal-melt element partitioning and basalt petrogenesis. Contributions to Mineralogy and Petrology 152, 685–702.

Watson, E.B., 1976. Two-liquid partition coefficients: experimental data and geochemical implications. Contributions to Mineralogy and Petrology 56, 119–134.

Wilson, M., Madden, P.A., 1993. Polarization effects in ionic systems from first principles. Journal of Physics: Condensed Matter 5, 2687–2706.

Wood, B.J., Blundy, J.D., 1997. A predictive model for rare earth element partitioning between clinopyroxene and anhydrous silicate melt. Contributions to Mineralogy and Petrology 129, 166–181.

Please cite this article as: Haigis, V., et al., Molecular dynamics simulations of Y in silicate melts and implications for trace element partitioning, Chem. Geol. (2012), http://dx.doi.org/10.1016/j.chemgeo.2012.08.021